electronic reprint

Journal of
Applied
Crystallography

ISSN 0021-8898

Editor: **Anke R. Pyzalla**

In situ ultra-small-angle X-ray scattering study of the solution-mediated formation and growth of nanocrystalline ceria

Andrew J. Allen, Vincent A. Hackley, Pete R. Jemian, Jan Ilavsky, Joan M. Raitano and Siu-Wai Chan

J. Appl. Cryst. (2008). **41**, 918–929

Copyright © International Union of Crystallography

Author(s) of this paper may load this reprint on their own web site or institutional repository provided that this cover page is retained. Republication of this article or its storage in electronic databases other than as specified above is not permitted without prior permission in writing from the IUCr.

For further information see http://journals.iucr.org/services/authorrights.html

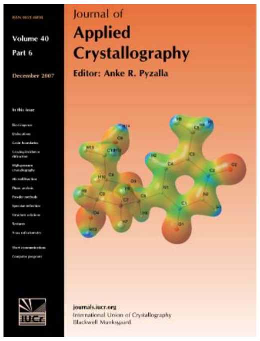

Many research topics in condensed matter research, materials science and the life sciences make use of crystallographic methods to study crystalline and non-crystalline matter with neutrons, X-rays and electrons. Articles published in the *Journal of Applied Crystallography* focus on these methods and their use in identifying structural and diffusion-controlled phase transformations, structure–property relationships, structural changes of defects, interfaces and surfaces, *etc.* Developments of instrumentation and crystallographic apparatus, theory and interpretation, numerical analysis and other related subjects are also covered. The journal is the primary place where crystallographic computer program information is published.

Crystallography Journals Online is available from **journals.iucr.org**

Journal of
Applied Crystallography
ISSN 0021-8898

Received 16 October 2007
Accepted 22 July 2008

In situ ultra-small-angle X-ray scattering study of the solution-mediated formation and growth of nanocrystalline ceria

Andrew J. Allen,[a]* Vincent A. Hackley,[a] Pete R. Jemian,[b] Jan Ilavsky,[c] Joan M. Raitano[d] and Siu-Wai Chan[d]

[a]Ceramics Division, National Institute of Standards and Technology, Gaithersburg, MD 20899, USA, [b]Engineering Support Division, Advanced Photon Source, Argonne National Laboratory, Argonne, IL 60439, USA, [c]X-ray Science Division, Advanced Photon Source, Argonne National Laboratory, Argonne, IL 60439, USA, and [d]Department of Applied Physics and Applied Mathematics, Columbia University, New York, NY 10027, USA. Correspondence e-mail: andrew.allen@nist.gov

Results are presented for an *in situ* synchrotron-based ultra-small-angle X-ray scattering (USAXS) study of the solution-mediated formation and growth of nanocrystalline ceria (n-CeO_2) using a new remote-controlled, isothermal, circulating fluid flow cell. The fluid flow mitigates or reduces X-ray beam-induced damage, air bubbles or particulate flocculation within the bulk solution, but prevents any coarse particulates that do form from settling out from suspension. Combined with the large-scale range accessible in USAXS studies, the flow cell has enabled measurement, *in situ* and in real time, of structural characteristics from 10 Å to a few micrometres in size as a function of the changing physical and chemical conditions. By applying a multi-component model, the nanoparticle formation and growth component has been identified. Control and online monitoring of flow rate, temperature and pH suspension conditions have permitted real-time studies of the formation and growth of the individual n-CeO_2 particles from homogeneous dilute solution over several hours. Aspects of the nanoparticle nucleation and growth are revealed that have not been observed directly in measurements on this system.

1. Introduction

The chemical and solid state properties of ceria, particularly nanocrystalline ceria (n-CeO_2), have resulted in its increased use in applications as diverse as solid oxide fuel cell electrolytes, superconductor and catalyst supports, semiconductor gate materials (Galata *et al.*, 2007) and wafer processing (Lee *et al.*, 2002), solar cells (Corma *et al.*, 2004), and even in healthcare (Schubert *et al.*, 2006). In order to provide sufficient quantities of material with a well controlled nanoparticle size distribution, 'soft chemistry' solution-mediated fabrication routes (Zhang *et al.*, 2002) have increased in importance, as has a consequent need to characterize the reaction products. Frequently, the technological challenge is to develop a sufficient understanding of the nanoparticle formation reaction process that will enable particles of controlled size and/or morphology to be harvested from suspension for specific applications.

While *ex situ* methods such as X-ray diffraction (XRD) and transmission electron microscopy (TEM) provide, respectively, the nanocrystalline phase information and nanoparticle morphology/size visualization for the forming reaction product, small-angle X-ray and neutron scattering (SAXS and SANS) methods are ideal for providing quantitative measurements of the statistically representative reaction product dimensions and morphology over the scale range from a few ångströms to several micrometres. In practice, the dilute nature of the reacting system calls for SAXS measurements to be made at an X-ray synchrotron source. Care must then be taken to mitigate any X-ray beam damage effects and to ensure that the material in the X-ray beam remains representative of the state of the reacting suspension. Furthermore, it is important to make measurements over a sufficiently wide range of length scales for the true nanoparticle nucleation and growth processes to be distinguished from other particle agglomeration effects.

In this context, the use of flow cells in SAXS studies of aqueous or other fluid samples presents several advantages (Amenitsch *et al.*, 1998; Hu *et al.*, 2000; Lipfert *et al.*, 2006). The fluid flow prevents settling out of coarse particulates from suspension. Control and online monitoring of the flow rate, temperature and suspension conditions (such as pH) enable real-time studies of solution-mediated processes to be made. Furthermore, the transient sampling of the sample material in fluid flow removes or mitigates the problem of bubble formation or sample modification that can occur in static suspensions exposed to the X-ray beam. This is especially true for the high-brilliance X-ray beams available at third generation synchrotron sources. Finally, the use of fluid flow presents a closer approximation, than does the use of sealed liquid cells, to the actual solution-mediated fabrication conditions for n-CeO_2 (or any of a number of nanoparticle systems) for which the reaction kinetics need to be explored and better understood.

This paper presents the application of a new isothermal fluid flow system (Hackley *et al.*, 2006) computer-interfaced with a Bonse–Hart ultra-small-angle X-ray scattering (USAXS) instrument – previously developed by some of the present authors with their collaborators (Long *et al.*, 1991, 2000; Allen *et al.*, 1994; Ilavsky *et al.*, 2002, 2004). By designing the automated fluid flow cell to be compatible with the USAXS computer control system, flowing fluid suspensions can be studied in real time, under known conditions of temperature, flow rate and pH (or any chemical species detectable by ion selective electrode), and over a scale range from 10 Å to a few micrometres, all within a single experiment.

In what follows, it will be shown how the real-time and monitoring capabilities of the cell can be exploited to study a nanoparticle formation reaction from solution under controlled conditions, and this paper presents the first results of a detailed USAXS study of solution-mediated n-CeO_2 formation. Aspects of the n-CeO_2 formation process are revealed that, to the best of our knowledge, have not previously been observed directly for this system. Finally, the applicability of SAXS flow cell methods to other advanced materials research is briefly discussed.

2. Experimental

2.1. USAXS studies using a circulating fluid flow cell

Details of the USAXS instrument, now located at sector 32-ID of the Advanced Photon Source (APS), Argonne National Laboratory, IL, USA, can be found elsewhere (Long *et al.*, 2000; Ilavsky *et al.*, 2002, 2004). Briefly, it is based on the Bonse–Hart instrument design and emphasizes advanced materials microstructure characterization from ~10 Å to a few micrometres. The instrument delivers ~10^{13} photons s^{-1} incident in a maximum 1 × 2 mm unfocused beam size at the sample position for 10 keV photons, an incident photon energy range from 7 to 18 keV using Si (220) crystal optics, a single-scan Q range from 0.0001 to 1 $Å^{-1}$ [where $Q = (4\pi/\lambda)\sin\theta$ and is the magnitude of the scattering vector, $\mathbf{Q}$, λ is the photon wavelength, and 2θ is the angle of scatter], over ten decades of detector linear intensity range, absolute intensity calibration by primary methods, and fluorescence rejection in the scattered beam. The facility offers semi-automated data reduction and rigorous data analysis using a range of structure factors and models.

The automated isothermal fluid flow system, designed for USAXS (or SAXS), is shown schematically in Fig. 1. Nominal set up for the apparatus includes a 1.5 mm-diameter quartz capillary X-ray cell (with a 10 µm wall thickness and flow perpendicular to the incident beam direction) enclosed in an isothermal compartment, an isothermal reaction vessel for sample mixing and titration, a dual-syringe automated burette for quantitative dosing, and a pump capable of maintaining uniform flow rates for extended periods. Temperature, flow rate and chemical dosing are remotely controlled and programmable through the USAXS instrument control system. Remote sensing of pH (or other ion-selective electrodes) and temperature allow precise control of the experimental conditions. The flow cell is compatible with a wide range of liquid media, including bio-relevant aqueous solutions and many common organic solvents. In the present experiments, the pump speed was set to yield a flow rate of 16 ml min^{-1}. Although the exact flow rate was not critical, this was sufficient to ensure that material would not settle out from suspension, to circulate fluid from the reaction vessel to the sample cell and back within about a minute, and to circulate the entire reaction fluid volume (300 ml) in less than 20 min. In addition, the dwell time of any one part of the sample fluid within the X-ray beam was only 3 ms for each pass, minimizing both bubbling due to X-ray beam damage and any effect this would have on the measurement. However, the flow rate was sufficiently low to give a Reynold's number of Re $\simeq$ 170, much less than the value (Re $\simeq$ 2000) needed to produce cavitation

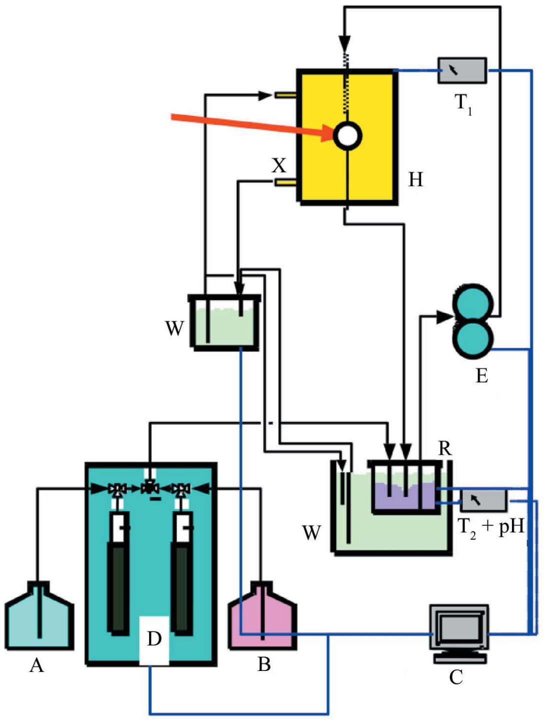

Figure 1
USAXS flow cell schematic, where A = feedstock A (*e.g.* acid); B = feedstock B (*e.g.* base); C = remote computer control; D = automatic dispenser; X = incident X-ray beam; H = isothermal capillary holder; T_1 = thermocouple for sample cell; W = water baths; E = peristaltic pump; R = reaction vessel; T_2 + pH = combined pH/temperature electrode for reaction vessel. Black lines indicate fluid flow both for sample and for temperature control; blue lines are computer control and sensor connections.

or bubbling as a result of turbulence or its associated shear effects on the particulate phase during transit (Rott, 1990).

To use the flow cell with the USAXS instrument, the X-ray undulator was tuned to give a typical X-ray energy of 10.5 keV (λ = 1.18 Å). This provided optimal beam flux and signal-to-noise ratio for flow cell measurements using an aqueous suspension. The beam size used in the experiments described here was 0.4 × 0.4 mm centered within the nominal 1.5 mm-diameter width of the capillary tube, giving minimal anisotropic distortion effects from the cylindrical sample shape. Since none of the measurements presented involved anisotropic scattering, the slit-smeared USAXS configuration was used. The scattering data were corrected both for parasitic background scattering effects and for attenuation using data from an aqueous buffer, absolute-calibrated with respect to the incident beam intensity, and desmeared using the well established Lake (1967) algorithm. In order to exploit the USAXS Q resolution and to relate, quantitatively, structures and phenomena at the nanoscale to those at the micrometre scale, Q was logarithmically stepped during the USAXS scan so as to provide an appropriate data-point weighting in Q over the extended Q range. Instrument dwell time at each of the 150 measured Q values needed to be sufficient to obtain reliable readings of both the USAXS photodiode detector current (for the scattering) and the ion chamber count rate for normalizing to the incident beam. Generally, a 5 s dwell time was more than sufficient. A typical scan, which includes motor movement and settling time, was completed in less than 25 min (see below), providing a time resolution well suited to the reaction fluid circulation time and the time dependence for n-CeO_2 formation.

2.2. Application to solution-mediated formation and growth of nanocrystalline ceria

For real-time studies of n-CeO_2 formation, cerium(III) nitrate hexahydrate [$Ce(NO_3)_3{\cdot}6H_2O$, 99.5% by mass] and hexamethylenetetramine [$(CH_2)_6N_4$, HMT, > 99% by mass], also known as hexamine or urotropine, were obtained (Alfa Aesar,[1] Ward Hill, MA) and used without further purification. Each chemical was dissolved separately in 150 ml of filtered deionized water in a polytetrafluoroethylene (PTFE) beaker to obtain the desired concentrations: 0.0375 *M* $Ce(NO_3)_3$ and 0.5 *M* HMT. Solutions were stirred magnetically for 30 min before being combined. The final solution was stirred continuously at a minimum rate during the reaction period.

HMT slowly decomposes in water to produce ammonia and formaldehyde (Strom & Jun, 1980):

$$\begin{gathered} C_6H_{12}N_4 + 6H_2O \rightarrow 6CH_2O + 4NH_3, \\ NH_3 + H_2O \rightarrow NH_4^+ + OH^-. \end{gathered} \tag{1}$$

This reaction is promoted in acidic media and leads to a gradual increase in solution pH due to the release of ammonia. Both the oxidation of Ce^{3+}, a weakly acidic metal cation with a pK_a of 8.3 (Baes & Mesmer, 1976), and the subsequent precipitation of cerium(IV) oxide are strongly pH sensitive:

$$Ce^{4+} + 2H_2O \rightarrow CeO_2 + 4H^+. \tag{2}$$

Immediately after the cerium nitrate and HMT solutions are mixed, the pH of the combined solution drops rapidly as Ce^{3+} ions are partially hydrolyzed and the reservoir of OH^- is consumed in the homogeneous formation of nuclei. Once the initial precipitation of CeO_2 occurs and steady-state growth begins, the pH slowly increases over a period of 24 h or more as HMT decomposition continues.

Experiments were conducted using a recirculating water bath with the isothermal reaction vessel and flow cell at 293, 298 and 308 K, all ±0.1 K. Solutions were initially prepared at room temperature (about 293 K), but the cerium nitrate solution was subsequently equilibrated at the experiment temperature within 10 min. Previous studies of this system (Zhang, Jin & Chan, 2004; Zhang, Wang *et al.*, 2004; Zhang *et al.*, 2002, 2006) using electron microscopy and both ultraviolet and X-ray spectroscopy methods have shown that, over several hours, n-CeO_2 precipitates out from solution with a well dispersed principal particle population consisting of single crystals of octahedral shape with eight {111} surfaces, or with an additional {200} surface-truncated octahedral shape. The single-crystal nature of the precipitating principal particles studied here is one element that distinguishes this system from other reported ceramic oxide nanoparticle formation studies, such as the SAXS study of ZnO formation by Tokumoto *et al.* (1999).

USAXS scans were made repeatedly on the flowing suspension as the n-CeO_2 formation reaction proceeded, while the temperature and pH in the reaction vessel, as well as the temperature at the sample measurement position, were continuously monitored. The scan time (also the time resolution) in these experiments was 23 min. Depending on the reaction temperature, the reaction was followed for between 5 h and more than 12 h from the time of mixing of the $Ce(NO_3)_3$ and HMT solutions, which initiates the principal reaction.

2.3. Additional experimental measurements

As discussed below, the USAXS data indicated the presence of not only a principal n-CeO_2 particle population, corresponding to that detected by other methods, but also a significant population of ultrafine features and small amounts of larger agglomerates. In order to determine the independence or otherwise of the fine features with respect to the principal population, particularly at later reaction times, one suspension was reacted for 331 min, then centrifuged for 30 min at 4000 r min^{-1} using a Sorvall Technospin R. The topmost portion of the supernatant was removed and measured by USAXS starting at just over 360 min from the start of the original formation reaction. For completely inde-

---

[1] Certain commercial materials and equipment are identified in this paper only to specify adequately the experimental procedure. In no case does such identification imply recommendation by NIST nor does it imply that the material or equipment identified is necessarily the best available for this purpose.

pendent particle populations, these parameters should have ensured near complete removal of the principal population, leaving primarily the fine features in suspension.

To elucidate further the scattering from the fine features observed in the USAXS studies, SANS measurements were carried out on a precipitating n-CeO_2 suspension. The component concentrations were doubled, so as to provide a measurable SANS intensity, and the suspension studied using a prototype SANS version of the fluid flow cell with the reaction temperature held at 297 K. Both the $Ce(NO_3)_3$ and the HMT solutions were prepared in D_2O to minimize the incoherent neutron scattering background from H_2O and also to exploit the significant scattering contrast between HMT and D_2O. The SANS measurements were carried out at the NIST Center for Neutron Research (NCNR), Gaithersburg, MD, using the NIST/Texaco/University of Minnesota NG7 SANS instrument (Glinka *et al.*, 1998). The SANS neutron wavelength, λ, was 6 Å and two different instrument configurations were used to obtain data over a Q range of $0.01 < Q < 1$ Å^{-1}. Data were recorded on a two-dimensional detector, corrected for detector sensitivity, electronic and parasitic background effects, and sample absorption, then calibrated against the incident beam flux and normalized to unit sample volume. Finally, the data were circularly averaged to obtain the absolute scattered intensity *versus* Q.

3. Analysis and size distribution results

3.1. Size distribution model for the ceria SAXS data

For particulate systems, one of the more useful software analysis tools is the entropy maximization algorithm *MaxEnt* (Potton *et al.*, 1988). From the data, it extracts a particle size distribution with logarithmically increasing bin size over the extended scale range. In the present case, *MaxEnt* was used for an initial exploration of the precipitating ceria size distributions and indicated the presence of up to four discrete component populations. However, although *MaxEnt* was useful for indicating the basic scattering feature populations present, in order to follow details of the n-CeO_2 formation and growth process as a function of reaction time and temperature, a more analytical approach was adopted. [See Ilavsky (2007) for computer algorithms in support of these and other USAXS/SAXS data reduction and analysis models.]

In order to model the scattering across the entire measured USAXS Q range, up to four separate volume-weighted particle size distribution components were required, each of standard lognormal form, $V_j(D)$ (*e.g.* Allen *et al.*, 1996; Filliben, 2006; Ilavsky, 2007):

$$\underset{j=1,4}{V_j(D)} = \frac{\varphi_{j\mathrm{TOTAL}}}{\left\{2\pi \ln\left[(D_{j\mathrm{MED}} - D_{j\mathrm{MIN}})/(D_{j\mathrm{MODE}} - D_{j\mathrm{MIN}})\right]\right\}^{1/2}} \times \left(\frac{1}{D - D_{j\mathrm{MIN}}}\right) \times \exp\left(\frac{-\left\{\ln\left[(D - D_{j\mathrm{MIN}})/(D_{j\mathrm{MED}} - D_{j\mathrm{MIN}})\right]\right\}^2}{2\ln\left[(D_{j\mathrm{MED}} - D_{j\mathrm{MIN}})/(D_{j\mathrm{MODE}} - D_{j\mathrm{MIN}})\right]}\right), \quad (3)$$

where $\varphi_{j\mathrm{TOTAL}}$ is the total volume fraction of particles in the jth population, and $D_{j\mathrm{MODE}}$ and $D_{j\mathrm{MED}}$ are its corresponding volume-weighted mode and median diameters, while $D_{j\mathrm{MIN}}$ is the minimum diameter for which the jth lognormal component applies. In following the formation and growth phenomena quantitatively as a function of the reaction time, it was found convenient to work with these component volume fraction size distributions rather than use the corresponding number-density size distributions. For each component, as well as following φ_{TOTAL}, D_{MODE} and D_{MED} as a function of the reaction time and temperature, the measured volume-weighted mean diameter, D_{MEAN} [also obtainable using the relation $(D_{\mathrm{MEAN}} - D_{\mathrm{MIN}}) = (D_{\mathrm{MED}} - D_{\mathrm{MIN}})^{3/2}/(D_{\mathrm{MODE}} - D_{\mathrm{MIN}})^{1/2}$], was followed. Finally, the number-weighted mean diameter for each component population, denoted D_{NO}, was followed for additional comparison with the model predictions. This is given by $(D_{\mathrm{NO}} - D_{\mathrm{MIN}}) = (D_{\mathrm{MODE}} - D_{\mathrm{MIN}})^{3/2}/(D_{\mathrm{MED}} - D_{\mathrm{MIN}})^{1/2}$.

The four lognormal components were separated in size, and the multi-component model enabled their separate dependences on the reaction time to be distinguished and quantified. The development of the two coarsest components could indicate the emergence of hierarchical particle morphologies. At extended reaction times of at least several hours, a mass- or volume-fractal structure was observed to develop at low Q (coarse length scales), evidenced by a Q power law with exponent between -2 and -3. This was possibly associated with the gradual formation of low-density agglomerates, as has been observed in some earlier SANS and SAXS studies of colloidal dispersions (*e.g.* Ottewill, 1991). However, the n-CeO_2 system remains very dilute even after reaction times of several hours, and it was recognized that the two coarsest components might also be associated with a gradual accumulation of ceria agglomerates on the quartz measurement cell under prolonged local exposure of the latter to the X-ray beam. Previous studies have indicated that the X-rays may locally oxidize Ce^{3+} to Ce^{4+} (Lapraz *et al.*, 2002), and this may enhance the gradual deposition of ceria on the quartz tube wall incident to the X-ray beam. To mitigate these effects, the sample cell was moved for each successive USAXS scan, so that no one part of the quartz measurement cell was irradiated for more than 25 min at a time. Nevertheless, as a precaution against agglomeration on the tube wall possibly contaminating results for the reacting suspension, each real-time reaction study was terminated once the apparent volume fraction for either of the two coarse populations became significant compared with that of the principal particle population. By fitting the four-component particle population model to the USAXS data over the entire Q range, it was possible to distinguish, and make detailed analysis of, the two fine (nanoscale) feature populations, which are of most relevance to developing an improved understanding of the solution-mediated n-CeO_2 formation reaction under fluid flow conditions. It was found that these two populations did not correlate with any observed local agglomeration on the quartz tube wall but could be associated continuously with the n-CeO_2 formation reaction within the flowing suspension.

Fig. 2(*a*) presents desmeared absolute-calibrated USAXS data across the whole Q range for the n-CeO$_2$ formed from solution in the flowing suspension at various mean times after initial mixing of the reactants, with the reaction vessel temperature held at 298 K. In addition to the principal particle population, A (with an assumed ceria density of 7100 kg m^{-3}), scattering from a prominent second population of ultra-fine features, B (also initially assumed to be ceria), was detected in the high-Q regime. Figs. 2(*b*) and 2(*c*) present the fitted volume fraction size distributions for these two populations, associated with the different Q ranges in the data and assuming the particle morphologies discussed below.

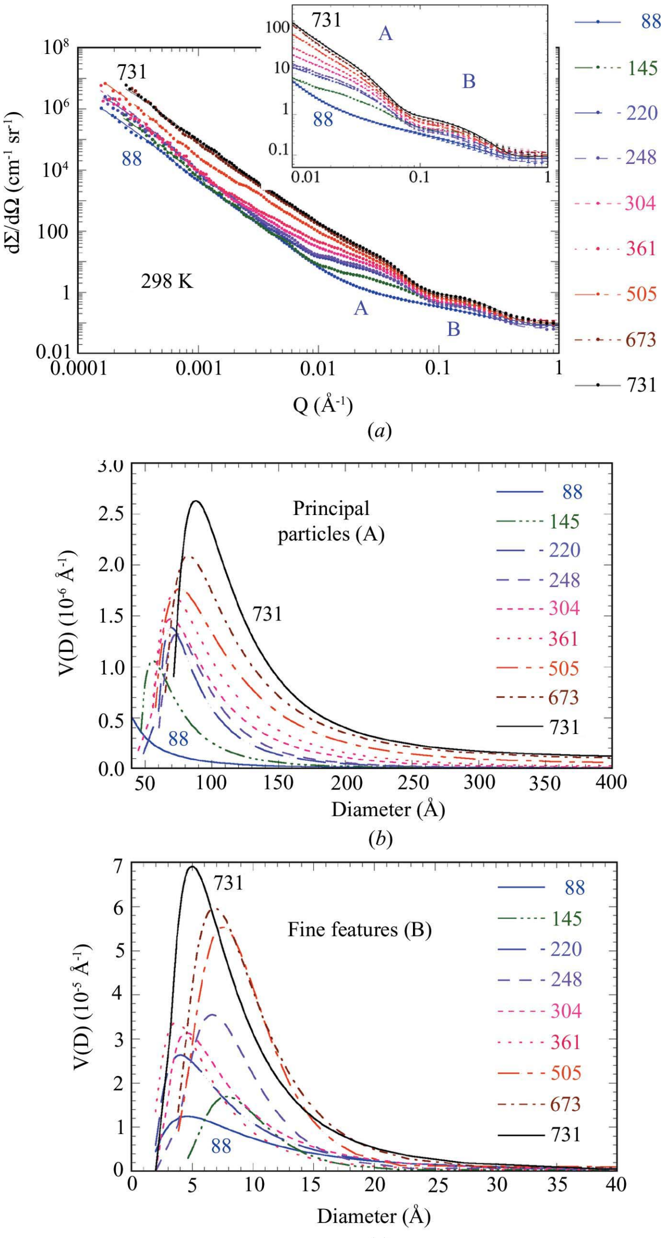

Figure 2
(*a*) Desmeared, calibrated USAXS data with multi-component lognormal size distribution fits for the precipitating n-CeO$_2$ suspension at 298 K. The inset expands the USAXS data regime associated with the size distributions A and B. The scatter in the intensity data indicates the statistical uncertainties, and the capped vertical bars in the inset (very small except at high Q) give the standard deviation uncertainties. (*b*) The fitted particle size distributions for the principal particle population (A). (*c*) The fitted size distributions for the fine feature population (B). The principal particle (A) and fine feature (B) populations are modeled as described in the text. Times are given in minutes from the point of mixing the Ce(NO$_3$)$_3$ and HMT solutions and are the mean times for specific USAXS scans.

3.2. Core–shell particle morphology

It is immediately apparent in Fig. 2 that the principal particle population (A), with a size well established in studies published elsewhere (Zhang, Jin & Chan, 2004), does not represent the finest features in the system, but that there is also an ultra-fine feature population (B) present. To allow for a cerium concentration gradient around the forming particles in this actively reacting system, instead of assuming a simple hard-sphere single-particle scattering form factor (Porod, 1982), a basic core–shell scattering form factor was used to model each of the nanoscale particle populations. A shell thickness, t_S, of 5 Å was assumed, together with a shell density of about half the ceria full density. These assumptions for the shell surrounding each n-CeO$_2$ particle were considered reasonable given the known association of HMT with ceria and the size of the cage-like structures it forms when complexed with cerium ions (see discussion below). The significant population of fine features, separated in size from the principal particle population, suggests a sub-critical nucleation size, perhaps with continuous precipitation and re-dissolution. A half-density shell provides a maximally sensitive, limiting-case representation of this effect.

The X-ray scattering length (or atomic form factor) densities for the core, ρ_C, and the solvent matrix, ρ_M, were chosen for fully dense CeO$_2$ and H$_2$O, respectively. They were deduced from the densities and tabulated values for X-ray atomic form factors (Chantler *et al.*, 2005), giving $\rho_C = 51.71$ and $\rho_M = 9.36$, both $\times 10^{14}$ m^{-2}. The shell value, ρ_S, was assumed to be 25×10^{14} m^{-2}. For a single population of core–shell features, the scattered intensity, $I(Q)$, is given by (Guinier & Fournet, 1955)

$$I(Q) = \frac{\varphi_C}{V_C}\left[\frac{3V_C(\rho_C - \rho_S)j_1(QR_C)}{QR_C} + \frac{3V_S(\rho_S - \rho_M)j_1(QR_S)}{QR_S}\right]^2, \tag{4}$$

where $j_1(x) = (\sin x - x\cos x)/x^2$, R_C is the core radius, R_S is the radius of the core plus shell (*i.e.* $R_S = R_C + t_S$), $V_C = (4\pi/3)R_C^3$, $V_S = (4\pi/3)R_S^3$ and φ_C is the volume fraction of the cores of the core–shell particles. For each population component the scattering was averaged over the size distribution, and the calculated contributions to the scattered intensity for each component were summed and fitted to the calibrated USAXS measured intensity data, dΣ/dΩ. The size distributions presented in Figs. 2(*b*) and 2(*c*) are for fully dense ceria cores of the principal particle population (A) and the fine feature population (B), respectively. The effect of assuming core–shells for the principal particle population (compared with assuming hard spheres) is modest (5–10% reductions in the volume fractions and diameters obtained); the effect on the fine feature population is stronger and significantly reduces the volume fraction from that obtained when assuming the particles to be hard spheres. The volume fraction of the fine feature cores would be further reduced if these in fact comprise high-density clusters of Ce^{3+} or Ce^{4+} ions complexed with the HMT structure. Conversely, their volume fraction would be significantly greater if the ion clusters associated with HMT have a low density. These possibilities are discussed further below.

4. Further results and discussion

4.1. Principal particle and fine feature formation and growth

Fig. 3 presents derived microstructure parameters for a precipitating n-CeO_2 suspension *versus* reaction time at 298 K. The volume fractions associated with both the principal particle population and the fine features (which have a larger apparent volume fraction at 298 K if assumed to be ceria) increase linearly with reaction time; however, only the principal population grows in size. The particle surface areas increase with the volume fractions, as do the particle number densities, although the latter are dominated by the fine particles in each population and hence show greater stochastics. All reaction runs are characterized by a drop in pH from the point of mixing, prior to the onset of the principal particle formation. The pH then gradually increases as the principal particle formation and growth progresses – attributable to the slow decomposition of HMT in association with the precipitation reaction.

Fig. 4 both summarizes our working assumption for the particle morphology of both populations and presents results from the centrifuge test carried out for 30 min after a reaction time of 331 min at 298 K. Since settling time in a centrifugal field is inversely proportional to the square of particle diameter (McCabe *et al.*, 1985), a significantly greater proportion of the principal population particles should be removed relative to that of the fine feature particles. Thus, after centrifuging for 30 min, the fine feature population should be enhanced if the principal and fine feature particles

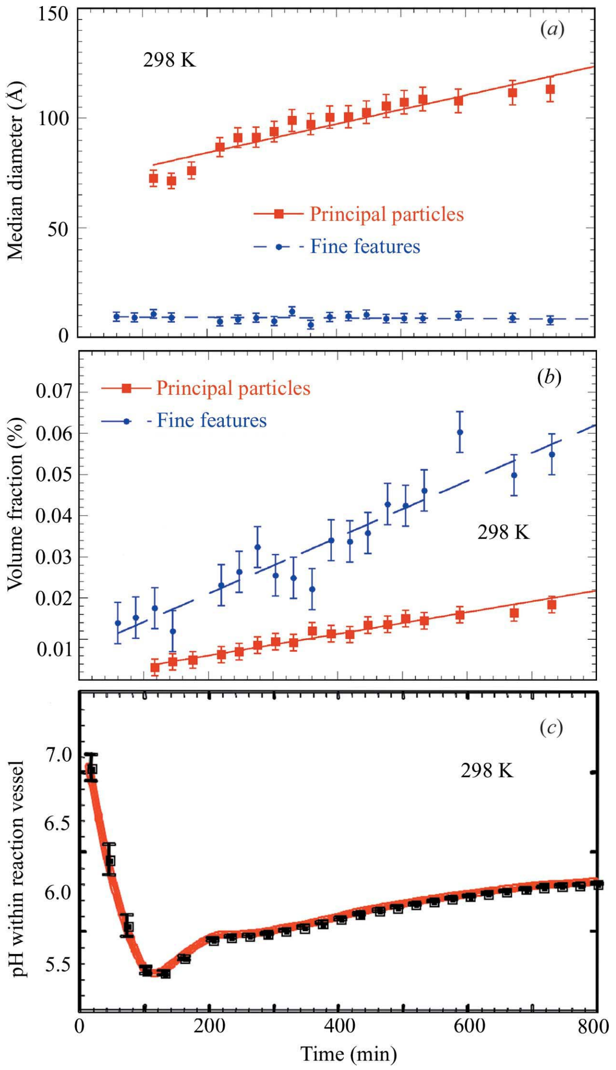

Figure 3
Derived microstructure parameters for a precipitating n-CeO_2 suspension *versus* reaction time at 298 K: (*a*) volume-weighted median diameters; (*b*) volume fractions; and (*c*) suspension pH. Straight-line fits are shown in (*a*) and (*b*). Capped vertical bars are estimated standard deviation uncertainties.

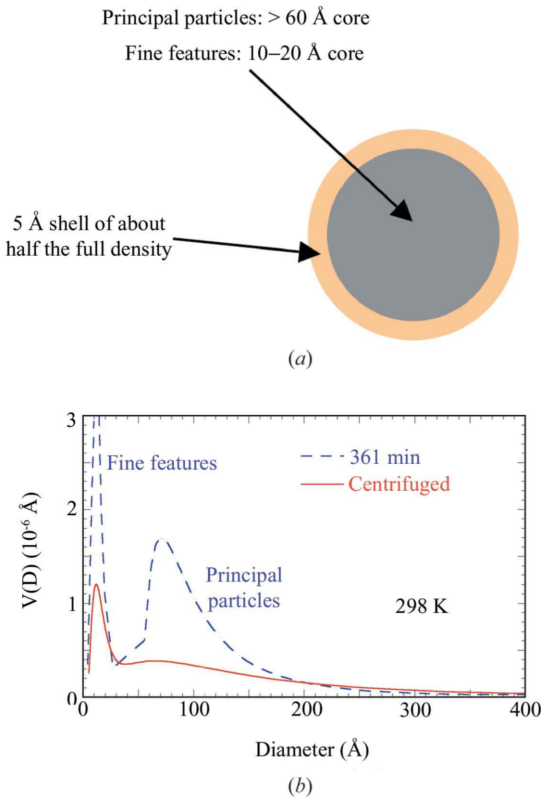

Figure 4
(*a*) Schematic showing the assumed n-CeO_2 particle core–shell morphology. For the principal particles, the shell is no more than a thin skin. However, for the fine features, the shell represents a significant fraction of the particle radius. (*b*) The effect on the feature size distributions of centrifuging the reacting n-CeO_2 suspension for 30 min after a 331 min reaction time, compared with an un-centrifuged suspension after 360 min reaction time.

Table 1
Particle volume fractions for n-CeO_2 after 360 min at 298 K, before and after centrifuging.

Suspension at 298 K	Apparent fine feature volume fraction (10^{-3}%)	Principal particle volume fraction (10^{-3}%)
After 6 h reaction	24.86 (50)	9.12 (50)
Centrifuged after 5.5 h	2.09 (50)	7.05 (30)

exist as separate entities. Clearly this is not observed: both populations are reduced but the reduction in the fine feature population is significantly more pronounced than that for the principal particle population (see Table 1). This strongly suggests that, once the principal particle population is established, the fine features are associated with the morphology of the principal particles, with the particle growth reaction itself, or with some other aspect of the suspension whether or not this is involved in the principal n-CeO_2 formation. In any case, the fine features are at least partially suppressed by the centrifugation process and do not appear to have a fully independent existence as ceria particles.

Further insight can be gained by following the reaction at a lower temperature, 293 K. Fig. 5(*a*) indicates a significantly slower time evolution of the scattering curves, and this is also apparent in the development of the volume fraction size distribution for the principal population, shown in Fig. 5(*b*). At 293 K, the onset of measurable principal particle formation occurs after 3 h and is characterized by a relatively abrupt growth in the volume fraction and size of the principal particles, from a diameter of less than 50 Å and a concentration level below the instrument's limit of sensitivity, to a mean diameter greater than 65 Å. Hints of this behavior are also present in the data obtained at the higher reaction temperatures of 298 and 308 K. Thus, the reaction is characterized by an initial induction period in which only fine features exist, followed by an abrupt onset of the principal particle development, where the latter grow rapidly from a fine nucleation size.

Notwithstanding these observations, it is an over-simplification to describe the development of the principal particle population solely in terms of its volume fraction and mean diameter. Fig. 6 shows that, as the n-CeO_2 formation reaction proceeds over early-to-intermediate times, the four previously defined population diameters, $D_{\rm NO}$, $D_{\rm MODE}$, $D_{\rm MED}$ and $D_{\rm MEAN}$, diverge, but at later times they seem to vary together, indicating a stable population width (particularly apparent at 298 K). Logarithmic fits to the data can be extrapolated back to the time that a discernible principal particle volume fraction can be detected. Although this means that diameter data are not available for the earliest reaction times, the logarithmic fits generally suggest rapid growth to the diameters indicated prior to the first time at which data are plotted. While only the reaction run at 298 K was followed out to an extended reaction time, the data indicate significantly greater initial broadening of the principal particle size distribution at higher temperatures. Starting from an initially narrow size distribution, the smaller diameters ($D_{\rm NO}$ and $D_{\rm MODE}$) derived from the size distribution grow slowly at later times and not at all at 308 K; the larger diameters ($D_{\rm MED}$ and $D_{\rm MEAN}$) continue to grow more rapidly, although not as rapidly as at early times. These trends represent a significant broadening of the principal particle size distribution. Extrapolating back to early reaction times, the distribution appears to grow and broaden from a single mono-dispersed particle diameter that itself has grown rapidly from a fine nucleation size. Once established, the behavior of the principal particle population is broadly in agreement with other measurements (Zhang, Jin & Chan, 2004). The lack of growth in the fine features suggests that they are associated structurally with the principal particles, rather than existing as an independent population. However, their existence in the period prior to the onset of a significant principal population (where the pH is decreasing rapidly) indicates that the fine features are more directly associated either with the precipitate formation process or with some other aspect of the suspension, rather than the principal particle product morphology itself.

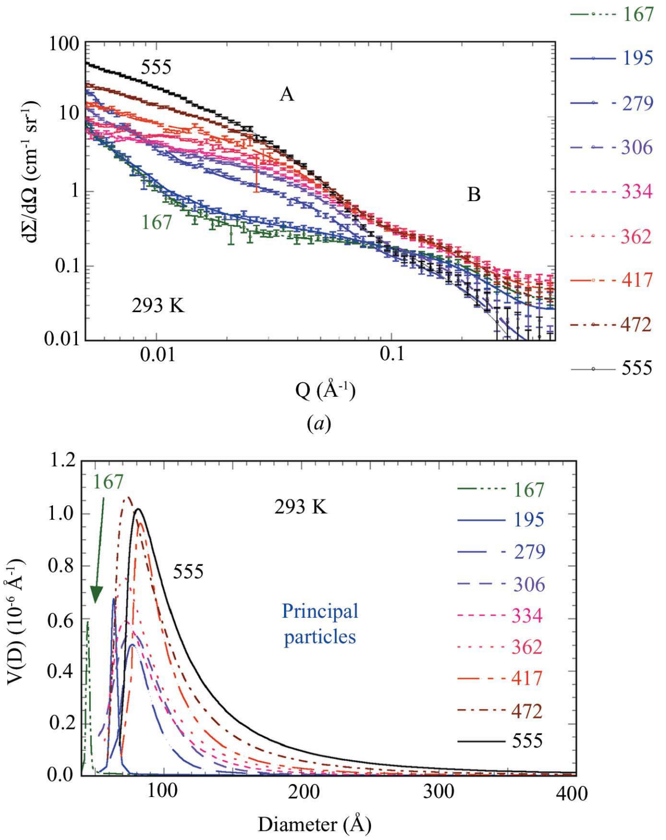

(*a*)

(*b*)

Figure 5
(*a*) Desmeared, calibrated USAXS data with multi-component lognormal size distribution fits for the precipitating n-CeO_2 suspension at 293 K. The scatter in the intensity data indicates the statistical uncertainties, and the capped vertical bars indicate the standard deviation uncertainties. Compared with the scattering from the principal particles (*A*), the scattering from the fine features (*B*) is significantly less prominent than at 298 K, and it is less certain with respect to the background scattering. (*b*) The fitted particle size distributions for the principal particle population. Times are given in minutes from the point of mixing the $Ce(NO_3)_3$ and HMT solutions and are the mean times for specific USAXS scans.

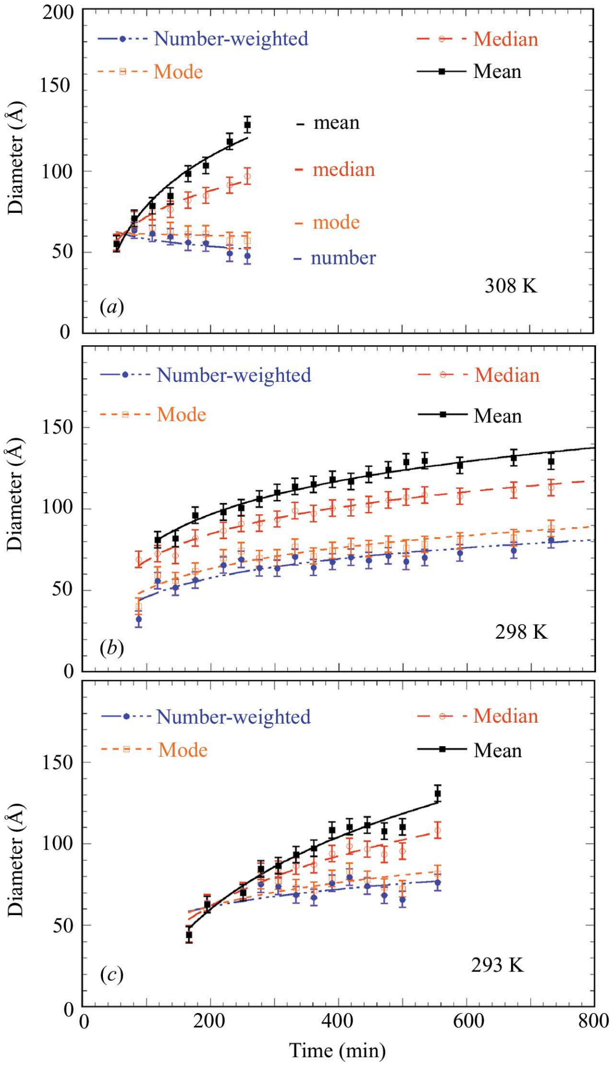

Figure 6
Volume-weighted mean, median and mode diameters, and number-weighted mean diameter for the principal particle population *versus* reaction time at (*a*) 308 K, (*b*) 298 K and (*c*) 293 K. Capped vertical bars are the estimated standard deviation uncertainties. The lines are logarithmic fits to the data, plotted from the time that a discernible principal particle volume fraction can be detected.

4.2. Temperature effects and the activation energy

The formation rate of n-CeO_2 from the reacting suspension was found to be a strong function of the reaction temperature. Fig. 7(*a*) presents the volume fraction *versus* reaction time for the principal population at 293, 298 and 308 K. Using these data, an Arrhenius plot, shown in Fig. 7(*b*), was derived to determine an activation energy of 49.1 (98) kJ mol^{-1}. It is important to note that this activation energy is associated with the n-CeO_2 principal particle formation *during the growth regime* for a solution-mediated reaction that proceeds at near room temperature. The value found is significantly lower than the few activation energies quoted in the literature for CeO_2 formation by other routes at elevated temperatures (*e.g.* Premkumar *et al.*, 2005). The same is true for solution-mediated nucleation of other species at or near room temperature (Burnham *et al.*, 2004), but the activation energy obtained here is comparable to that quoted in the same study for solution-mediated particle growth (29.3 kJ mol^{-1}).

At 308 K, the n-CeO_2 formation occurs rapidly, and the fine features are less prominent than at 298 K. However, just as at 293 and 298 K, the mean diameter of the fine feature cores remains between 5 and 10 Å, and it does not vary with either reaction time or temperature, as discussed further below. Fig. 7(*c*) presents the ratio of the fine feature to principal feature volume fractions as a function of reaction time, from the point where the principal population becomes measurable. From this figure, it can be inferred that the initial ratio is large, even at the highest reaction temperature, and is larger still at lower reaction temperatures. However, in all cases at extended reaction times, this ratio decreases to the order of unity, and less for the reaction at 308 K. This same ratio is also significantly reduced for the sample centrifuged after 330 min reaction time at 298 K. Meanwhile the principal particle population shows evidence of a universal growth law in $D_{\rm MED}$, once this has exceeded 66 Å, as shown in Fig. 7(*d*). Data from the reaction runs at all three temperatures studied fall on a universal curve with a median diameter growth rate of 2.12 (24) Å min$^{-1/2}$. This means that, at the different reaction temperatures, the steady-state reaction rate after several hours must be largely determined by the principal particle nucleation rate during the relatively brief period when the principal population first becomes detectable.

4.3. Interpretation of the fine feature population

Despite the significant apparent volume fraction of fine features detected in these experiments, no significant yield of n-CeO_2 particles below 20 Å in diameter has been obtained from this formation reaction. Principal particles can be harvested from the suspension once the onset of the principal particle population has occurred, and, for a brief period, these may be as small as 40 Å in diameter. However, the diameter of particles harvested increases rapidly to 65 Å, as shown in Figs. 2, 5 and 6. Thereafter, the diameter of the particles obtained increases slowly with reaction time, consistent with the results of the experiments presented in Figs. 3, 6 and 7(*d*). The existence of an independent fine feature population is not supported by the results of the centrifuge experiment. If the fine features existed as an independent particle population, centrifuging as previously described should have enhanced their relative prominence, not suppressed it as observed. Thus, the fine features must be associated (i) with the principal particle morphology, (ii) with the formation and growth reaction itself, or (iii) with some other aspect of the suspension that may, or may not, be involved in the principal n-CeO_2 particle formation. Furthermore, at least in cases (ii) and (iii), the individual fine features may be transient in nature.

With respect to the morphology of the principal particles, we recall that these are faceted single crystals. While a 5 Å shell of half the full ceria density can be justified in terms of an incoming flux of Ce^{3+} ions, explanation of the fine features in terms of an extended shell of tens of ångströms around each principal particle is not supported by other evidence in the available literature, and acceptable fits to the scattering data are not obtainable using such an extended core–shell morphology. Furthermore, comparison of the fine features with the principal population, as a function of both reaction time and temperature, does not support their interpretation as part of the principal particle morphology. During the reaction, the fine features are present prior to the onset of a detectable principal population and, while the fine feature size does not vary (Fig. 3*a*), their volume fraction relative to that of the principal particle population (Fig. 7*c*) does vary as a function of both reaction time and temperature. Equally, a direct association of (perhaps transient) fine features with the formation reaction itself is not supported. The fine feature volume fraction increases linearly with time from the initiation of the reaction, unlike the principal volume fraction which increases linearly from a later time. Thus, the fine feature volume fraction is not linearly related to the reaction rate for the principal particles, which would be zero for an initial induction period and would then rise to a constant value once the onset of the principal particle precipitation has occurred. By contrast, there is evidence that the fine features may arise from an association between cerium ions and structures within the HMT suspension.

HMT is a tertiary amine with a rigid adamentane-like cage structure (Blazevic *et al.*, 1979). As a potential tetradentate ligand, HMT can exhibit different coordination modes in complexing metal ions to produce a rich landscape of one-, two- and three-dimensional supramolecular architectures (Zhang *et al.*, 1999; Moulton *et al.*, 2001; Zheng *et al.*, 2003). Furthermore, the sizes of such complexes are generally consistent with the 10–15 Å size range found here for the fine features. Thus the ability of HMT to form bridged polynuclear structures with metal ions is well established and suggests the possibility of such formation in the present system involving Ce^{3+}. The self-assembly of such proto-crystalline structures could play a key role in the formation and growth of n-CeO_2. Additionally, oxidation of Ce^{3+} to Ce^{4+} is promoted in a basic environment (Izu *et al.*, 2006), and although the slow hydrolysis of HMT provides a controlled source of hydroxyl groups to sustain the oxidation and precipitation reactions, HMT is thought to play a more explicit role since this change in

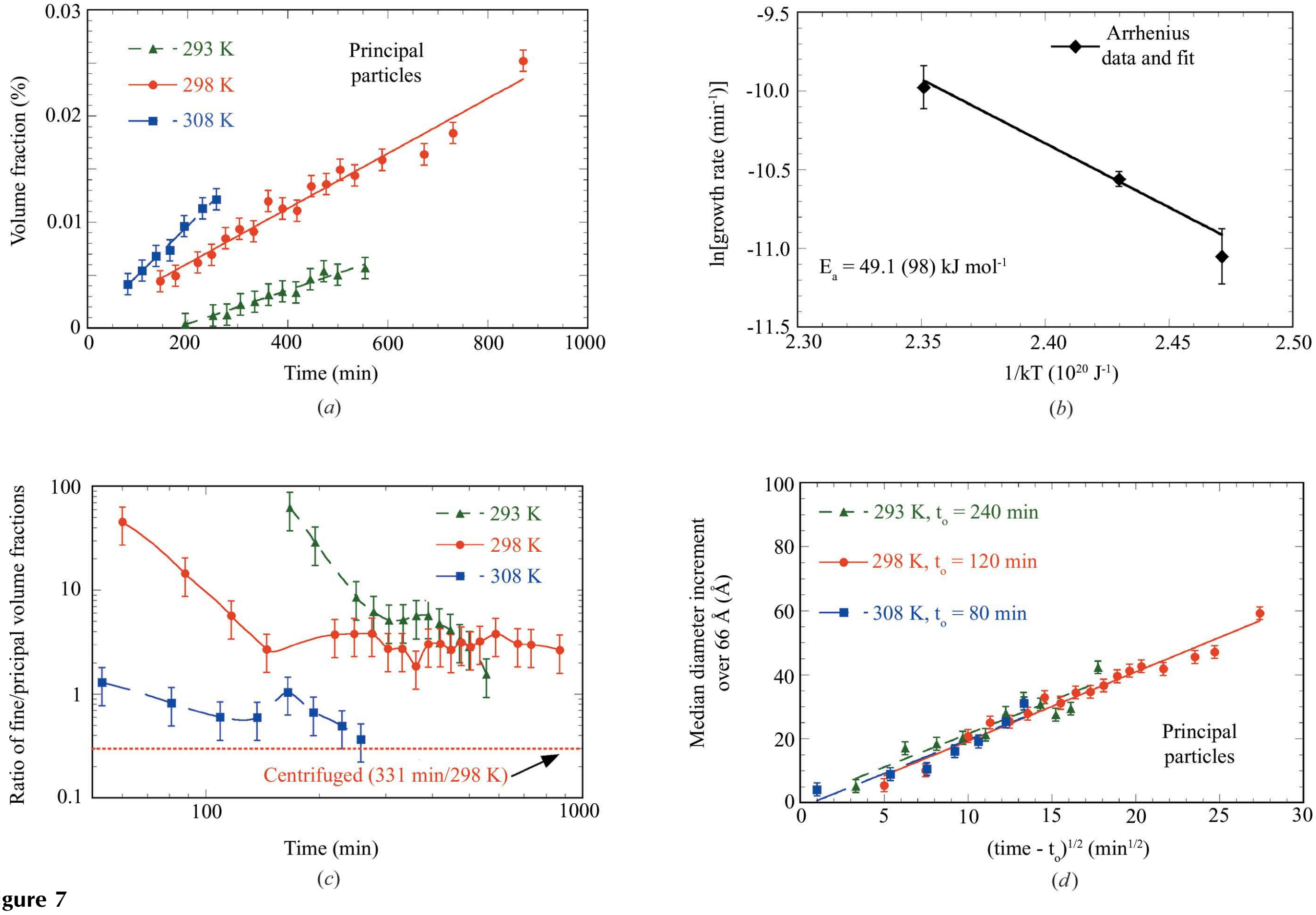

(*a*) (*b*)

(*c*) (*d*)

Figure 7
(*a*) Principal particle volume fractions *versus* reaction time at 293, 298 and 308 K, with straight line fits giving growth rates of 1.59 (28), 2.59 (12) and 4.65 (63), respectively, all $\times 10^{-5}$% min^{-1}. (*b*) Arrhenius plot derived from (*a*), giving an activation energy for growth of the principal particle population of 49.1 (98) kJ mol^{-1}. (*c*) Ratio of the fine feature/principal particle volume fractions *versus* reaction time. (*d*) Median principal particle diameter increment greater than 66 Å *versus* the square root of the reaction time increment greater than the time, t_o, when the median diameter first attains 66 Å. The nearly coincident straight lines indicate universal growth behavior for the individual nanoparticles. Capped vertical bars are the standard deviation uncertainties.

valence state of cerium also occurs with HMT in an acidic environment (Chen & Chen, 1993). This is analogous to HMT facilitating the oxidation of alkyl halides to aldehydes in the Sommelet reaction (Blazevic *et al.*, 1979). Close proximity of the HMT and cerium ions would promote this process further and could serve as a template to facilitate a high local concentration of cerium ions. Further support for complex formation between Ce^{3+} and HMT is found in the analysis of n-CeO_2 particles that have been harvested and dried after undergoing homogenous precipitation. Unpublished results based on thermogravimetric and elemental analysis of these precipitates suggest that sub-monolayer residues of HMT remain attached to the nanocrystalline surface (Wong-Ng & Cook, 2002). Furthermore, in the solution-mediated formation of ZnO nanoparticles and nanowires, HMT has been implicated as a surface-active structure-directing molecule (Sugunan *et al.*, 2006; Ismail *et al.*, 2005).

In the case of ceria, it is not clear from the current literature how the formation of cage-like complexes of HMT with Ce^{3+} or Ce^{4+} can be related directly to the HMT structure itself, particularly for a solution of HMT in water. However, solid crystalline HMT has been determined to have a cage-like structure with a unit-cell parameter of around 7 Å (Terpstra *et al.*, 1993). Fig. 8 presents evidence from small-angle neutron scattering (SANS) measurements that the fine features do indeed arise from an association between cerium and structures within the HMT solution. Fig. 8 shows calibrated SANS data in the high-*Q* regime both for the HMT solution prior to mixing with the cerium nitrate solution and for the combined suspension after several hours. In both cases the suspension is in D_2O rather than H_2O in order to minimize the strong incoherent scattering background from H_2O. While SANS data from H_2O or D_2O, or the $Ce(NO_3)_3$ solution in D_2O, are virtually flat as a function of *Q*, with no significant SANS component, the data from HMT show a structure that resembles closely the SANS data in the fine-feature high-*Q* regime for the reacting suspension. In SANS, the scattering contrast factor between HMT and D_2O is roughly four times that between CeO_2 and D_2O (see Table 2), and the molar HMT concentration is much higher than for cerium or ceria. Thus, while the HMT structure is detectable in SANS, the SANS signal is not significantly enhanced by any subsequent association or templating of cerium with the HMT structure at a relatively small number of sites. Interestingly, a *MaxEnt* size distribution analysis of the SANS data in Fig. 8 gives a mean feature diameter of ~14 Å. This is larger than the unit-cell parameter of 7 Å for the solid HMT cage structure but is consistent with the fine feature core size distributions of Fig. 2(*b*) if the SANS result is assumed to include the shell thickness. In SAXS or USAXS, the scattering contrast for CeO_2 in H_2O is about 350 times stronger than that between HMT and H_2O (and even stronger for a more concentrated cluster of Ce^{3+} or Ce^{4+} ions). The HMT structure itself is too weak to be detectable in the SAXS studies, but the fine HMT/Ce^{3+} or HMT/Ce^{4+} complexes should become detectable as cerium increasingly associates with a relatively small fraction of HMT sites and shows up in SAXS data as the fine feature population.

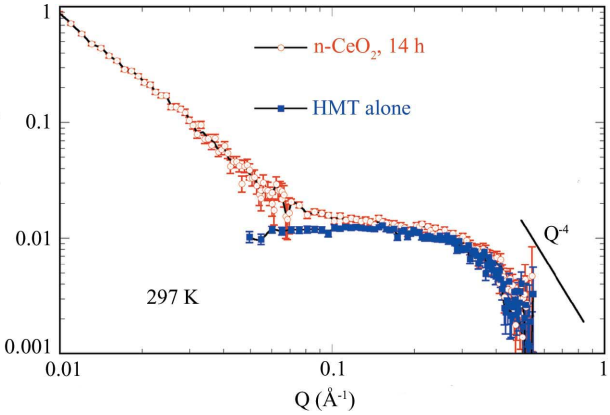

Figure 8
Calibrated SANS data *versus* *Q* for a precipitating n-CeO_2 suspension at 297 K, together with corresponding data for the HMT solution alone. (After background subtraction, the data for HMT using the low-*Q* instrument configuration are too stochastic to be plotted but do not exhibit any structure with *Q*.) Lines are guides to the eye. After flat background subtraction at high *Q*, a Q^{-4} Porod scattering exponent is found for both n-CeO_2 and HMT as indicated. Capped vertical bars are the standard deviation uncertainties.

Table 2
Calculated SAXS and SANS scattering contrast factors.

Phase	SAXS contrast factor with H_2O (10^{28} m^{-4})†	SANS contrast factor with D_2O (10^{28} m^{-4})‡
CeO_2	1793.52	5.29
HMT	6.35	21.07

† Chantler *et al.* (2005). ‡ Sears (1992).

In the context of the studies presented here, progressive clustering of Ce^{3+} and later Ce^{4+} ions, templated to the HMT structure within the suspension, is consistent with this being a precursor to the principal particle nucleation, which occurs once a critical precursor concentration has been attained (depending on temperature and pH). In principle, development of both the principal particle and the fine feature populations can be analyzed in terms of an Avrami nucleation and growth model (Avrami, 1939, 1940, 1941). However, the reaction time constants found are too long (and uncertain), with respect to the reaction times studied, for the results of such an analysis to be useful; the increase in either reaction product volume fraction remains linear with reaction time. Throughout the reaction time studied, the principal population volume fraction, although increasing, remains significantly less than the maximum possible ceria volume fraction of 0.045% for the reactant concentration used. Similarly, the fine feature volume fraction, if interpreted as a ceria-decorated complex with HMT, remains much less than the maximum possible precipitated HMT volume fraction of 2.70% based on the HMT concentration used.

Some aspects of the precursor phenomenon were observed in the ZnO SAXS study previously cited (Tokumoto *et al.*, 1999). However, the formation reaction here is different, and the fine precursor features are more prominent relative to the principal particle population. After extended reaction times, this same phenomenon becomes the precursor for principal particle growth, rather than nucleation, without itself changing significantly as a process. Any significant association of HMT/Ce^{3+} and HMT/Ce^{4+} complexes with the particle surfaces would justify the assumption of 5 Å half-density shells around the principal n-CeO_2 particles. For the fine features themselves, the 5 Å shell is simply indicative of the dynamic nature of sub-critical formation and re-dissolution processes. While some aspects of the solution-mediated n-CeO_2 formation and growth reaction have been inferred previously, to the best of our knowledge, the fine feature/precursor phenomenon has not been directly observed in previous studies of the solution-mediated formation of n-CeO_2.

5. Conclusions

A new automated fluid flow cell for USAXS or SAXS studies has been described and demonstrated. Its use in USAXS experiments has been presented for the real-time *in situ* study of a solution-mediated n-CeO_2 formation reaction. For the principal particle population, real-time studies at different temperatures have enabled the activation energy to be measured for nanoparticle growth. Above ~66 Å in diameter, the individual nanoparticles exhibit universal growth behavior, independent of the reaction temperature. Further work is needed in order to understand more fully how solution-mediated n-CeO_2 formation may be controlled and optimized. In particular, future SAXS and SANS work in the high-Q regime will be needed to explore the precursor phenomenon comprehensively for both this and other systems. If this fine feature population could be observed in other HMT-mediated homogeneous precipitation reactions, involving different metal ion reacting species, this would lend credence to the hypothesis that HMT plays an active role in the formation and growth process (in addition to its passive role in modifying pH). The present results have confirmed many aspects of the principal particle formation observed elsewhere, but, as far as we are aware, the presence of the fine or precursor features has not previously been observed directly and identified with respect to the HMT structure and its overall role in the formation and growth process.

Currently, other flow cell applications include characterization of the dispersion quality in single-walled and multi-walled carbon nanotube suspensions relevant to electronic and biomedical applications, measurement of dispersion quality in metal/ceramic nanoshell composites for cancer therapy, and characterization of self-assembled nanostructures for drug delivery. Frequent requirements are the need to work with small suspension volumes (< 10 ml) and low particle concentrations (< 0.1% volume). Extension of the flow cell capabilities to meet these requirements is underway, as is development of corresponding facilities for SANS experiments.

We thank C. Amigo of NIST Ceramics Division for critical support in the design and construction of the flow cell holder, A. Jilla, formerly of NIST Ceramics Division, for help with the initial flow cell concept, and J. Gordon of the Department of Applied Physics and Applied Mathematics, Columbia University, New York, for assistance in the data analysis. Use of the Advanced Photon Source is supported by the US Department of Energy, Office of Science, under contract No. W-31-109-ENG-38. Part of this work utilized instrumentation supported by the NIST Center for Neutron Research. S-WC and JMR are supported by the MRSEC Program of the National Science Foundation (DMR-0213574), the New York State Office of Science, Technology and Academic Research (NYSTAR), and the Department of Energy under BES/HFI grant No. DE-FG02-05ER15730.

References

Allen, A. J., Jemian, P. R., Black, D. R., Burdette, H. E., Spal, R. D., Krueger, S. & Long, G. G. (1994). *Nucl. Instrum. Methods Phys. Res. Sect. A*, **347**, 487–490.

Allen, A. J., Krueger, S., Skandan, G., Long, G. G., Hahn, H., Kerch, H. M., Parker, J. C. & Ali, M. N. (1996). *J. Am. Ceram. Soc.* **79**, 1201–1212.

Amenitsch, H., Bernstorff, S., Kriechbaum, M., Lombardo, D., Mio, H., Pabst, G., Rappolt, M. & Laggner, P. (1998). *Nuovo Cimento Soc. Ital. Fis. D*, **20**, 2181–2190.

Avrami, M. (1939). *J. Chem. Phys.* **7**, 1103–1112.

Avrami, M. (1940). *J. Chem. Phys.* **8**, 212–224.

Avrami, M. (1941). *J. Chem. Phys.* **9**, 177–184.

Baes, C. F. Jr & Mesmer, R. E. (1976). *Hydrolysis of Cations.* New York: Wiley Interscience.

Blazevic, N., Kolbah, D., Belin, B., Sunjic, V. & Kajfez, F. (1979). *Synthesis*, **3**, 161–176.

Burnham, A. K., Weese, R. K. & Weeks, B. L. (2004). *J. Phys. Chem. B*, **108**, 19432–19441.

Chantler, C. T., Olsen, K., Dragoset, R. A., Kishore, A. R., Kotochigova, S. A. & Zucker, D. S. (2005). *X-Ray Form Factor, Attenuation and Scattering Tables* (Version 2.1), http://physics.nist.gov/ffast.

Chen, P.-I. & Chen, I.-W. (1993). *J. Am. Ceram. Soc.* **76**, 1577–1583.

Corma, A., Atienzar, P., Garcia, H. & Chane-Ching, J. Y. (2004). *Nat. Mater.* **3**, 394–397.

Filliben, J. J. (2006). *Exploratory Data Analysis*, in *NIST/SEMATECH e-Handbook of Statistical Methods*, edited by C. Croarkin & P. Tobias, p. 1.3.6.6.9, http://www.itl.nist.gov/div898/handbook/.

Galata, S. F., Evangelou, E. K., Panayiotatos, Y., Sotiropoulos, A. & Dimoulas, A. (2007). *Microelectron. Reliab.* **47**, 532–535.

Glinka, C. J., Barker, J. G., Hammouda, B., Krueger, S., Moyer, J. J. & Orts, W. J. (1998). *J. Appl. Cryst.* **31**, 430–445.

Guinier, A. & Fournet, G. (1955). *Small-Angle Scattering of X-rays.* New York: John Wiley.

Hackley, V. A., Allen, A. J., Jemian, P. R., Raitano, J. M. & Chan, S.-W. (2006). *Growth of Nanocrystalline Ceria Studied Using a USAXS Capillary Flow-Cell, Proceedings of the 5th World Congress on Particle Technology.* New York: AIChE. (Available on CDROM.)

Hu, M. Z. C., Zielke, J. T., Byers, C. H., Lin, J. S. & Harris, M. T. (2000). *J. Mater. Sci.* **35**, 1957–1971.

Ilavsky, J. (2007). *APS 32ID-B USAXS Ultra-Small-Angle X-ray Scattering Facility*, http://usaxs.xor.aps.anl.gov/docs/overview/links.html.

Ilavsky, J., Allen, A. J., Long, G. G. & Jemian, P. R. (2002). *Rev. Sci. Instrum.* **73**, 1660–1662.

Ilavsky, J., Jemian, P. R., Allen, A. J. & Long, G. G. (2004). *Versatile USAXS (Bonse–Hart) Facility for Advanced Materials Research. Eighth International Conference on Synchrotron Radiation Instru-*

mentation, AIP Conference Proceedings 705, edited by A. Warwick, J. Arthur, H. A. Padmore & J. Stohr, pp. 510–513. Melville: American Institute of Physics.

Ismail, A. A., El-Midany, T. A., Abdel-Aal, E. A. & El-Shall, H. (2005). *Mater. Lett.* **59**, 1924–1928.

Izu, N., Itou, T., Shin, W., Matsurbara, I. & Murayama, N. (2006). *J. Ceram. Soc. Jpn*, **114**, 418–420.

Lake, J. A. (1967). *Acta Cryst.* **23**, 191–194.

Lapraz, D., Prevost, H., Iacconi, P., Guigues, C., Benabdesselam, M. & Briand, D. (2002). *Radiat. Prot. Dosim.* **100**, 365–368.

Lee, S.-H., Lu, Z., Babu, S. V. & Matijevic, E. (2002). *J. Mater. Res.* **17**, 2744–2749.

Lipfert, J., Millett, I. S., Seifert, S. & Doniach, S. (2006). *Rev. Sci. Instrum.* **77**, 046108.

Long, G. G., Allen, A. J., Ilavsky, J., Jemian, P. R. & Zschack, P. (2000). *The Ultra-Small Angle X-ray Scattering Instrument on UNICAT at the APS, Synchrotron Radiation Instrumentation: Eleventh US National Conference*, edited by P. Pianetta, J. Arthur & S. Brennan, pp. 183–187. Melville: American Institute of Physics.

Long, G. G., Jemian, P. R., Weertman, J. R., Black, D. R., Burdette, H. E. & Spal, R. (1991). *J. Appl. Cryst.* **24**, 30–37.

McCabe, W. L., Smith, J. C. & Harriott, P. (1985). *Unit Operations of Chemical Engineering*, p. 904. New York: McGraw–Hill.

Moulton, B., Lu, J. & Zaworotko, M. J. (2001). *J. Am. Chem. Soc.* **123**, 9224–9225.

Ottewill, R. H. (1991). *J. Appl. Cryst.* **24**, 436–443.

Porod, G. (1982). *Small-Angle X-ray Scattering*, edited by O. Glatter & O. Kratky, pp. 17–51. London: Academic Press.

Potton, J. A., Daniell, G. J. & Rainford, B. D. (1988). *J. Appl. Cryst.* **21**, 663–668.

Premkumar, T., Govindarajan, S., Coles, A. E. & Wight, C. A. (2005). *J. Phys. Chem. B*, **109**, 6126–6129.

Rott, N. (1990). *Ann. Rev. Fluid Mech.* **22**, 1–11.

Schubert, D., Dargusch, R., Raitano, J. & Chan, S. W. (2006). *Biochem. Biophys. Res. Commun.* **342**, 86–91.

Sears, V. F. (1992). *Neutron News*, **3.3**, 29–37.

Strom, J. G. Jr & Won Jun, H. (1980). *J. Pharm. Sci.* **69**, 1261–1263.

Sugunan, A., Warad, H. C., Boman, M. & Dutta, J. (2006). *J. Sol-Gel Sci. Technol.* **39**, 49–56.

Terpstra, M., Craven, B. M. & Stewart, R. F. (1993). *Acta Cryst.* A**49**, 685–692.

Tokumoto, M. S., Pulcinelli, S. H., Santilli, C. V. & Craievich, A. F. (1999). *J. Non-Cryst. Solids*, **247**, 176–182.

Wong-Ng, W. & Cook, L. (2002). Unpublished data.

Zhang, F., Chan, S. W., Spanier, J. E., Apak, E., Jin, Q., Robinson, R. D. & Herman, I. P. (2002). *Appl. Phys. Lett.* **80**, 127–129.

Zhang, F., Chen, C. H., Raitano, J. M., Hanson, J. C., Caliebe, W. A., Khalid, S. & Chan, S. W. (2006). *J. Appl. Phys.* **99**, 084313.

Zhang, F., Jin, Q. & Chan, S. W. (2004). *J. Appl. Phys.* **95**, 4319–4326.

Zhang, F., Wang, P., Koberstein, J., Khalid, S. & Chan, S. W. (2004). *Surf. Sci.* **563**, 74–82.

Zhang, Y., Li, J., Xu, H., Hou, H., Nishiura, M. & Imamoto, T. (1999). *J. Mol. Struct.* **510**, 191–196.

Zheng, S.-L., Tong, M.-L. & Chen, X.-M. (2003). *Coord. Chem. Rev.* **246**, 185–202.